Torres Górriz, B.; Calderón García, PA.; Paya-Zaforteza, I.; Sales Maicas, S. (2014). Experimental and numerical analysis of a hybrid FBG long gauge sensor for structural health monitoring. Measurement Science and Technology. 25:1-15. doi:10.1088/0957-0233/25/12/125107.

This paper presents a new long gage sensor for Structural Health Monitoring based on the use of Fiber Bragg Gratings. The proposed sensor has the advantage over existing sensors that it does not require prestressing of the optical fiber. The development consisted of numerical studies complemented by experimental tests to analyze: (1) the strain transfer between the sensor and the host structure; (2) the influence of sensor axial stiffness on the structural behavior of the host structure; (3) the influence of the mechanical properties of the adhesive used to fix the sensor; and (4) the failure modes of the sensor (buckling and shear stress of sensor anchors).

Notation

A, B	Points that define sensor length by coordinates $X_B - X_A$
A_s	Cross-sectional area of sensor unit.
C	Mid-point of sensor by coordinates $X_C = {(X_A + X_B)}/{2}$
c_s	Cohesion of concrete/adhesive contact surface according to the Mohr-Coulomb failure criterion.
E_A	Adhesive elasticity modulus.
E_C	Concrete elasticity modulus.
E_s	Elasticity modulus of sensor unit material.
E_N^S	Elasticity modulus perpendicular to concrete/adhesive contact plane.
E_P^S	Elasticity modulus of concrete/adhesive contact plane.
f_c	Concrete compressive strength
f_t	Uniaxial out of plane yield stress according to the *3-D Elasto–Plastic Interface Model* criterion implemented on Lusas FE code.
f_{yk}	Steel yield limit of specimen reinforcement.
f_{ys}	Steel yield limit of specimen head reinforcement.
G_N^S	Out of plane shear modulus in the plane of contact between concrete and adhesive
G_P^S	In plane shear modulus in the plane of contact between concrete and adhesive.
I_s	Moment of inertia of long gage sensor unit.
K	Stiffness of buckling inhibitor.
u_b, u_A	Displacements in direction X of points A and B after deformation of long gage sensor.
x_b, x_a	Coordinates of points that define sensor length.
$\varepsilon_{x,s}(X)$	Strain distribution along X axis between anchors A and B (Glisic 2011, [24]).
$\varepsilon_{C,s}$	Strain distribution between anchors A and B attributed to middle point C (Glisic 2011, [24]).
λ_B	Reflected Bragg wavelength.

ν_N^S	Poisson coefficient perpendicular to concrete/adhesive contact plane.
ν_P^S	Poisson coefficient contained in concrete/adhesive contact plane.
τ_i	Shear stress at concrete / adhesive interface.
τ_u	Maximum shear stress on contact surface according to Mohr-Coulomb failure criterion.
σ_i	Normal stress on contact surface according to Mohr-Coulomb failure criterion.
ϕ_s	Angle of friction on contact surface according to Mohr-Coulomb failure criterion.
$\Delta w_{d,i}$	Dimension changes in the interval bounded by $X_B - X_A$ due to cracking, changes in size of air pockets, etc. in X direction after deformation (Glisic & Inaudi 2007).
CFRP	Carbon Fiber Reinforced Polymer
FBG	Fiber Bragg Grating.
ΔL_s	Increase in sensor length.
L_s	Sensor length.
$\varepsilon_{c,EXP}$	Experimental strain on specimen concrete as measured by reference point sensor.
$\varepsilon_{s,EXP}$	Experimental strain on specimen concrete as measured by long gage optical sensor.
$\varepsilon_{c,FEM}$	Theoretical strain on specimen concrete obtained from 3D FE model.
$\varepsilon_{s,FEM}$	Theoretical strain on long gage sensor obtained from 3D FE model.
$\varepsilon_{C,0,FEM}$	Theoretical strain on specimen concrete without long gage sensor obtained from 3D FE model
P_{RD}	Load at which buckling occurs in long gage sensor.
$P_{RD,3.5}$.	Load on long gage sensor corresponding to a 3.5‰ bending-axial strain.

Experimental and numerical analysis of a hybrid FBG Long gauge sensor for Structural Health Monitoring.

Notation: See attached document.

1- Introduction.

Strain is one of the most important parameters to monitor when assessing the state of a structure. Although strain can be measured by different methods, fiber optics is at present one of the most advanced technologies in this field, due to its advantages over other types of sensor and the reduction in its price. These advantages relate mainly to their flexibility, embeddability, multiplexity, small size and immunity to electrical or magnetic interference [1, 2, 3].

With reference to their spatial disposition, fiber optic sensors used to measure strains are classified as distributed (or continuous) sensors or discrete (or point) sensors. Distributed sensors measure the parameter at several positions in the fiber and can replace a chain of point measurements whereas discrete sensor measures a parameter related to a single position in the structure between two given points. The distance between these two points is known as "gauge length" and defines the length of the sensor.

Discrete sensors can be classified into "long gauge" and "short gauge" according to their gauge length. The choice of the correct type will depend on the objective of the study and on the nature of the material involved in the test [1]. Traditional sensors such as strain gauges belong to the "short gauge" group and measure strains between two points quite close together, of the order of a few millimeters, so that the values they register are highly influenced by any local defects or irregularities in the study zone. Such sensors are suitable for monitoring homogeneous materials like steel. However, other types of material such as concrete, wood, stone, or composites such as CFRP (Carbon Fiber Reinforced Polymer) may have local defects or irregularities, including cracks, cavities and air pockets. These materials need to be monitored by long gauge sensors that give the mean strain value between two points far enough apart not to be influenced by local irregularities. Long gauge sensors range in length from a few centimeters to several meters and give an overall picture of the behavior of the structure. They can also be built into the structure during the construction stage (e.g. in the case of concrete elements) or placed on the surface of the structural element as it might be the case in existing buildings, wooden structures and historical buildings [1].

Regardless of the principle on which it is based (Bragg gratings, interferometry, etc.) or its type of installation (embedded or surface mounted) the working of a long gauge fiber optic sensor requires that it be prestressed in order to measure compression strains correctly. Due to its low degree of stiffness, if optical fiber has not been prestressed, it may buckle even at relatively small compression loads. All the presently available long gauge fiber optics sensors (e.g. [4], [5]) have prestressed fibers and generally give satisfactory results in a variety of applications ([1], [6], [7], [8]). However, prestressing the fiber is a delicate operation with an uncertain outcome that is best avoided, due to: 1) some conditions (e.g. fibers slipping in their anchorage, temperature variations, etc.) could cause loss of prestressing and lead to erroneous measurements; 2) the level of prestressing is normally not known; 3) the prestressing operation may damage the fiber; and 4) developing fiber optics strain sensors able to work at high temperatures requires non prestressed sensors, since high temperatures cause the fibers to dilate, neutralize the initial prestressing and cause fiber deformation.

In addition, sensors need a special packaging that enables the optic fiber to be fixed to a structure without influencing the strain field or structural displacements of the host structure, while at the same time ensuring the correct transmission of structural strains to the fiber. Examples of different types of packaging with materials such as steel or composites can be found in Calderón & Glisic [8], Torres et al [9], Majumder et al. [10], Li et al. [11], Moyo et al. [12], Leng et al. [13], Kesavan et al. [14] and [15]. It should also be pointed out that using a proper packaging is a crutial issue in sensors development since previous research [16] reported discrepancies between the measured and actual strain values that have been attributed to the choice of packaging.

In this context, this paper proposes a new design for a surface-mounted long gauge sensor that does not require prestressing of the optical fiber to function correctly. The aim of this paper is to identify, for proposed long gauge sensor, the critical parameters that influence the accuracy of the strain measurement, to study how these parameters affect the accuracy, and to give recommendations for sensor users. The sensor study was based on: 1) a series of experimental tests on concrete elements subjected to simple compression designed to verify the functioning of the sensors; 2) finite element numerical models to: 2.i) quantify the influence of the mechanical and geometrical properties of the proposed packaging (anchorage, length of sensor, packaging stiffness) when measuring strains; 2.ii) assess the interaction of the sensor with the structure under study; 2.iii) optimize the sensor design in order to keep measurement errors to a minimum; and, 2.iv) study all the possible failure modes of a surface-mounted sensor. Eliminating fiber prestressing gives the sensor a substantial advantage over other sensors available at the present time and opens the way to the development of fiber optic sensors able to measure strains at very high temperatures that might be very useful in fire engineering and in the power plants.

2- Proposed long gauge fiber optic sensor.

The working principle of the proposed sensor is based on the use of FBGs (Fiber Bragg Gratings). An FBG is a reflector built in a short segment of the core of an optical fiber by exposing the fiber to an intense UV light. This exposure creates periodic alterations in the index of refraction of the fiber core, known as Bragg gratings, and makes the FBG (1) reflect only particular narrowband light wavelengths of light known as Bragg wavelengths, and (2) transmit all others (see Fig. 1), as shown in [17]. The Bragg wavelength condition is given by Eq. (1), where λ_B is the wavelength of the FBG, n_{eff} is the effective refractive index of the fiber core, and Λ is the Bragg grating period or distance between two consecutive alterations of the fiber core [9].

$$\lambda_B = 2\, n_{eff} \Lambda \tag{1}$$

As external perturbations such as strains and temperature changes induce modifications in the Bragg grating period Λ, they also induce a shift $\Delta\lambda_B$ in the Bragg wavelength. Using a calibration, it is possible to separate both perturbations to obtain strain and temperatures by measuring the Bragg wavelength shift.

The design of the proposed long gauge sensor can be seen in Fig. 2. The optical fiber is anchored at both ends to the mid-point of a linear element fixed by adhesive to the structure to be monitored. It is considered that the strain on the linear element is uniform at all points throughout its length and also that Eq.(2), as shown by Glišić & Inaudi [1], gives the direct value of the mean strain between the sensor's two anchorage points, $\varepsilon_{C,s}$. In Eq.(2) $\varepsilon_{x,s}(x)$ represents the strain distribution between anchorage points A and B, ΔL_s represents the increase in sensor length, L_s the sensor length, u_B and u_A

the displacements in direction X of points A and B after deformation of long gage sensor, X_B and X_A the coordinates of points that define sensor length, $\Delta w_{d,i}$ the number and magnitude of discontinuity (e.g. air pockets, cracks, etc.) between A and B, and L_s is the sensor length.

$$\varepsilon_{C,s} = \frac{\Delta L_s}{L_s} = \frac{u_B - u_A}{x_B - x_A} = \frac{1}{L_s}\int_{x_A}^{x_B} \varepsilon_{x,s}(x)\,\mathrm{d}\,x + \frac{1}{L_s}\sum_i \Delta w_{d,i} \tag{2}$$

The following points should be considered in designing a sensor:

1. The linear element should be subjected to the same strains as the structure under study. The design of the sensor anchors and the properties of the adhesive material are fundamental to achieving this aim [9].

2. Fixing a sensor to a structure can interfere with the strains in the monitored zone, as explained in Section 5.1. Proposed long gauge optical sensor unit must have sufficient axial stiffness, so that the sensor does not influence the strain of the host structure. To achieve a low value of axial stiffness, aluminum material has been chosen to manufacture linear element.

3. The length of the sensor depends on the structure and the nature of the study to be carried out. The proposed sensor unit is prismatic, with a rectangular cross section and variable length. Tests were carried out with sensor lengths of between 0.2 and 1 m.

4. This proposed long gauge sensor must able to function correctly under all types of strain. However, it could buckle under small compression loads because proposed sensor has to be as slender as possible to avoid interfering with structural strains. For this reason, corrective measures have to be designed to ensure its stability. The sensor design includes a component that acts as a buckling inhibitor. This component restricts movements of the sensor and this prevents its buckling. Buckling inhibitor increase bending stiffness but not modify the value of axial stiffness. Buckling inhibitor design will be explained and described later, on 5.2.2.

3-Experimental study of sensor

In order to test the sensor in practical applications, a set of experiments were carried out on concrete specimens subjected to compression. The proposed sensors were mounted on the surface of the structural element. The strains measured by the sensors were compared to the values provided by the point fiber optic sensors described in [9], placed close together. Different types of specimen were produced in order to test different sensor lengths.

Experimental tests have been performed in laboratories under controlled environmental conditions (temperature and humidity). Due to the short duration of the tests, temperature and humidity have remained constant during the tests, so temperature effect on FBG and packaging has not been considered in this article.

3.1 Characteristics of the specimens used

Three types of concrete specimens were produced for use in the experiments:

1. Specimen A (see Fig.4a). Prismatic mass concrete specimens with a 0.10 m x 0.40 m cross section.

2. Specimen B (see Fig. 4b). Prismatic mass concrete specimens with a 0.20 m x 1.20 m cross section.
3. Specimen C (see Fig. 4c). Prismatic mass concrete specimens with a 0.30 m x 3.00 m cross section.

The column heads (load application zones) shown in Figs. 4b and 4c had to be reinforced to avoid local failure due to compression stresses. The reinforcement took the form of a steel jacket to confine the concrete in this area. The load applications were increased and reduced gradually in all the tests until the concrete gave way. The different types of specimen and the tests to which they were subjected can be seen in Table 1.

3.2 Properties of materials used in the tests

The concrete specimens were made from different mixes since the tests were carried out at different times. In the three cases, both compression strength and elasticity modulus were determined by simple compression tests on standardized 0.15 m diameter x 0.3 m high cylindrical specimens by the procedure described in [18].

Specimen A was made with high resistance concrete. Table 2 summarizes the main mechanical properties at 28 days obtained in the tests on three standardized cylindrical specimens. Mean values of the compression strength f_{c28} and elasticity modulus were 100.4 MPa and 34116 MPa, respectively.

Specimens B and C were made with a conventional concrete and gave mean compression strength and elasticity modulus values of 7.1MPa and 29450 MPa. Table 3 gives the values obtained from the tests on the three standardized cylindrical specimens. Note that a compression strength value could not be obtained for the third specimen due to a problem with the data acquisition system. The yield strength of the steel used in the reinforcement was $f_{yk} = 500$ MPa and that of the metal jacket used to reinforce the column heads was $f_{ys} = 265$ MPa.

3.3 Test frames

The tests were carried out in the laboratory of the Concrete Science and Technology Institute (ICITECH in Spanish) of the Universitat Politècnica de València (UPV).

Specimen A shown in Fig. 4a was tested in an ICON press with an automatic control system and a maximum load of 2500 kN, connected to a computer system for data capture and storage.

Specimen B shown in Fig. 4b was tested in a 2 m high metal frame equipped with a hydraulic jack with a load capacity of 2500 kN. The specimen was supported on a base considered to be infinitely stiff consisting of three solid metal sheets 0.10 m thick. The load was applied to the top of the structure until the specimen fractured.

Specimen C in Fig. 4c was tested in another metal frame 3.5 m high and 5000 kN maximum load. As in the preceding case, the columns were placed on supports considered to be infinitely stiff and a vertical load was applied to the head until collapse occurred.

3.4 Instrumentation

Point fiber optic sensors developed by Torres et al. [9] were placed alongside the proposed new optical sensors in all the tests to validate the results obtained.

The interrogation system used for the strain monitoring was an FBG type *MicronOptics*, *Model sm125-500* and a laptop computer with software developed specifically for this application [19] in *LabVIEW*^{TM} V. 8.5 programming language. The sm125-500 optical sensing interrogator is composed of a tunable *Fabry-Perot* laser source with a wavelength range of 1510 to 1590 nm and four optical channel outputs. Maximum data capture frequency is 1 Hz and measurement precision is 1 pm. The laptop used in the tests was an Intel Pentium 4 a 2.4 GHz with 768 MB Ram.

Load cells were used to record the loads applied by the hydraulic jack. This data was handled in real time by a *Pentium IV* computer. The data acquisition equipment was a *Hewlett Packard Model HP 3852* and the acquisition software was programmed in *LabVIEW*^{TM}.

4-Numerical model

Numerical 3D finite element models of the sensor-structure assembly were created with the *Lusas* program [20], with the aim of: 1) quantifying the effect on the measurements of the mechanical and geometrical properties of the proposed sensor (sensor anchoring, lengths and stiffnesses); 2) evaluate the interaction of the sensor with the monitored structure; 3) optimize sensor design to minimize measurement errors; and 4) study possible failure modes of the sensor when placed in or on a structure (shear stress on the anchorage of the sensor to the structure, sensor buckling under compression loads).

4.1 Description of the finite elements used, boundary conditions, and load application.

The different elements figuring in the study were modelled: concrete, adhesive, sensor and optical fiber. Concrete, adhesive and sensor were modeled by hexahedric finite elements with 20 nodes and three degrees of freedom per node (element HX20). Optical fiber was modeled with BRS3 linear elements [20] with three nodes and three degrees of freedom per node (translations along the three X, Y and Z axes). Fig. 5 gives the finite elements used, all of which have non-linear elastic behavior. As the concrete specimens were supported on solid steel bases that were supposed to be infinitely stiff, translations were forbidden in all the axes of the nodes of the specimen bases. Loads were applied to the top of the specimen and were increased until the load levels of the laboratory experiments were reached.

4.2 Concrete-adhesive interface

The concrete-adhesive interface with the structure was simulated by HX20 hexahedric elements (Fig. 5). The constitutive model employed was the 3-D Elasto–Plastic Interface Model [21], implemented on Lusas, which allowed a friction plane between two 3-D bodies to be considered. The elastic properties (E, G and υ) were defined for two axes, one on the contact interface and another perpendicular to it. Failure occurred in the concrete-adhesive interface when any of the following conditions was met:

- The *Mohr-Coulomb* failure criterion, shown in Eq.(3), was satisfied:

$$\tau_u = c_s + \sigma_i \, tag\phi_s \quad (3)$$

(Variables of Eq.(3) are defined in the Notation Section.)

- Normal stress at the interface reached a uniaxial out of plane yield stress of f_t. When this value was reached, the sensor lost its attachment to the host structure due to normal tensile stresses.

The properties assigned to the concrete-adhesive interface are summarized in Table 4, which indicates the interface's elasticity modulus, cross-sectional stiffness module, and Poisson coefficient (identified as E_P^S, E_N^S, G_P^S, G_N^S,υ_P^S and υ_N^S respectively), both on the contact interface (subscript "*P*") and in the direction perpendicular to it (subscript "*N*"). The table also gives the values of the parameters necessary for the *Mohr-Coulomb* failure criterion, i.e. cohesion of the contact interface c_s and its angle of friction ϕ_s as well as the value of f_t .

Concerning Table 4, it is important to note the following:

- The same elastic properties values (E, G and υ) were considered for the contact interface and the direction perpendicular to it [21].
- The values assigned to the contact interface were obtained from the mean value of the two elements in contact [21], i.e. concrete and adhesive.
- The value adopted for cohesion (c_s) is 10 MPa, which represents the adhesive manufacturer's shear strength value.
- The friction angle (ϕ_s) assumed is 0. The numerical model results do not depend on this value, since there are no normal forces on the contact interface.
- A value of 35 MPa was adopted for f_t (uniaxial out of plane yield stress). This value was also provided by the adhesive manufacturer.

4.3 Buckling study

In the buckling study, the sensor element was modeled by thin shell QSL8 elements (Fig. 5), with 8 nodes [18] and:

- Three degrees of freedom (translations in the X, Y and Z axes) in the element's corner nodes.
- Five degrees of freedom (three translations and two turns) in the element's side nodes.

Buckling was studied by an Eigenvalue analysis carried out on Lusas [20], which provides the theoretical buckling strength of a structure which is idealized as elastic.

5- Results and discussion

5.1 General behavior

5.1.1 Transmission of strains

The sensor was mounted on the surface of the Specimen A, as shown in Fig. 4, fixed at both ends by a two-component adhesive. The specimens were submitted to compression loading-unloading cycles. The strain values measured by the reference point optic sensor were compared to those recorded by the proposed long gauge sensor.

Fig. 6 gives the values of the experimental strains in concrete $\varepsilon_{c,EXP}$ as measured by the reference sensor and those measured by the proposed long gauge sensor (continuous blue and black lines, respectively). It also shows the values of the theoretical strains in concrete $\varepsilon_{c,FEM}$ and in the long gauge sensor $\varepsilon_{s,FEM}$ obtained from the numerical 3D finite element model (with markers and dotted line). Finally, the continuous maroon-colored line indicates the proposed loading-unloading cycle, with a maximum load value of 225 kN.

The results given in Fig. 6a show that the strains are not entirely transmitted from the concrete to the sensor (as can be seen in Fig.6b), since the sensor records lower strains than the concrete (the sensor/concrete strain ratio $\varepsilon_{s,FEM}/\varepsilon_{c,FEM}$ is around 0.75, or a 25% difference). In the numerical model it can be seen that these differences are due to the mechanical properties of the adhesive. The property with most influence on sensor behavior is the adhesive's elasticity modulus E_A.

The effect of the adhesive's elasticity modulus E_A on the $\varepsilon_{s,FEM}/\varepsilon_{c,FEM}$ ratio (Fig. 7) was studied with the above numerical model. The results show that there is a minimum value E_A = 400 MPa, after which the $\varepsilon_{s,FEM}/\varepsilon_{c,FEM}$ ratio is almost 1, and the total strain is transmitted from the concrete to the sensor unit. However, at small E_A values (around 90 MPa) there is incomplete strain transmission, with $\varepsilon_{s,FEM}/\varepsilon_{c,FEM}$ ratios close to 0.75 and a 25% difference between the real strain values and those measured by the sensor.

After discovering the importance of the properties of the adhesive for transmitting strains between concrete and sensor, another experimental test was designed with the same loading-unloading cycles but with a different adhesive of E_A = 13000 MPa. The results are given in Fig. 8 and confirm that total strains are transferred from concrete to sensor ($\varepsilon_{s,FEM}/\varepsilon_{c,FEM}$ ratios very close to 1) and therefore that the sensor is working correctly.

5.1.2 Axial stiffness of the sensor

The long gauge optical sensor unit must have sufficient axial stiffness, E_sA_s, E_s being the sensor material's elasticity modulus, and A_s its cross section, so that the sensor does not influence the strain of the host structure. The influence of this value was assessed by FEM from the ratio between the strain in the concrete with no sensor, $\varepsilon_{C,0,FEM}$, and that of the concrete plus sensor, $\varepsilon_{C,FEM}$. Fig. 9 shows the relationship between the axial stiffness of the element E and the $\varepsilon_{C,0,FEM}/\varepsilon_{C,FEM}$ ratio for sensors 20, 40 and 60 cm long.

Fig. 9 shows that the influence of sensor axial stiffness is reduced for longer sensor lengths. This influence can also be assessed graphically from the concrete's displacement field in the Y-direction (load application axis) (Fig.10). Thus, in Fig. 10a the influence of the sensor element can be clearly seen, as its axial stiffness $E_s A_s$ is high. In this case, the displacement isolines in the specimen are no longer horizontal. In Fig. 10b there is no sensor element on the surface and the displacement isolines are horizontal.

5.2 Sensor failure modes

The set of experiments carried out demonstrated the existence of two possible sensor failure modes:

a) Separation of the sensor from the concrete due to shear stress at the sensor element/concrete interface.

b) Buckling of the sensor during operation.

These failure modes and the methods of avoiding them were analyzed in a special study with 3D FE numerical models on Lusas. Lusas models had the characteristics described in sections 4.2 and 4.3 in relation to the studies on ultimate shear stress and buckling respectively.

5.2.1 Study on ultimate shear stress

The proposed sensor causes a local increase of the shear stresses at the sensor/concrete interface. If these stresses reach the threshold value (as defined by the *Mohr-Coulomb* failure criterion) the sensor unit separates from the concrete.

Fig. 11 shows the experimental strains in the concrete and sensor obtained in a compression test of Specimen C and the theoretical strains of concrete and sensor obtained from the 3D FE model. It can be seen that the sensor fails around minute 28.8 because it separates from concrete (Fig. 12). Up to the time of failure, the strains measured by the long gauge sensor were compared to the concrete strains obtained from the reference point fiber optic sensor, and the behavior was quite similar (less than 5% of difference in the strain values). As the load value was increased, there are greater differences between the experimental and theoretical values, which could be attributed to possible bending of the column due to the load not being perfectly centered in the experiments, while in the numerical model it was.

This experiment also enabled to calibrate the numerical model by comparing the numerical and experimental strains and thus to determine the shear stresses at the adhesive/host structure interface (Fig.12). First row in Table 5 indicates: the time at which the sensor separated from the structure, the main sensor characteristics, and the numerical results obtained, including: shear stresses at the adhesive/concrete interface τ_i, concrete strain in the direction of the applied load $\varepsilon_{c,FEM}$, and sensor strain $\varepsilon_{s,FEM}$. According to Fig 12b the separation of the sesnsor from the concrete specimen took place when the shear stress on the contact interface was 12.04MPa. This value was recorded at the upper corners of the interface, as shown in Fig. 12b, and is similar to the adhesive's maximum shear strength value entered in the numerical model as cohesion value.

It is important to note that an elasto-plastic model was used to simulate the contact interface. However, as the separation that actually occurred was sudden, the numerical model adopted is therefore only valid for estimating shear load values at the interface up to separation time.

In the light of the above results, in order to guarantee the correct operation of the long gauge sensor it was found necessary to adopt measures to reduce the shear stresses, for which two alternatives were studied:

a) A decrease of the adhesive's elasticity modulus, E_A.

The evolution of shear forces is in direct relation with the E_A value adopted. The numerical model clearly shows that the higher the E_A value, the greater the horizontal stresses generated in the contact interface (Fig.13).

However, reducing the adhesive's elasticity modulus E_A has a negative effect on the transfer of strains between the structure and concrete, as explained in Section 5.1.1, so that this method was ruled out as a solution to the problem.

b) Reducing the sensor element cross section A_S.

Smaller cross section area implies lower shear stresses in the contact interface. The sensor element's cross section was therefore reduced by 50%, after which a study was made of the horizontal loads in the contact interface by means of an FE numerical model.

Second row in Table 5 gives a summary of the main numerical results obtained. Fig. 14 shows the value of the shear stresses on the concrete under the same load conditions in which failure occurred in Fig. 12b.

After reducing the cross section area by 50%, the maximum shear stress value at the contact interface for a concrete strain of -979.5 με is 6.15 MPa (Fig. 14), as against the previous value of 12.04MPa. This means that the operation of the sensor/concrete interface is considerably improved and rules out the separation of the two elements, since the new maximum shear stress is lower than f_t .

After making a numerical estimation of the value of the shear forces reached in the experimental tests, these were repeated with 50% less cross section area in the sensor.

The results obtained are given in Fig. 15, in which the deformation obtained with the long gauge sensor is compared with the concrete deformation (obtained from the reference point sensor), placed at a short distance from the long gauge sensor. In this test, the concrete failed after 8.75 minutes at a concrete strain of 2‰, which is understandable since the specimen was under simple compression. After about 6.5 minutes, and therefore before concrete failure, the specimen was unloaded in order to detect a possible hysteresis associated with the load/unload of the sensor element. The sensor element did not become detached during the test and showed the same strain as the concrete, measured by a reference optical point sensor (Fig.15). The results show an excellent degree of fit and the behavior of the long gauge sensor is considered to be very satisfactory.

5.2.2 Sensor buckling study

The proposed sensor had to be as slender as possible to avoid interfering with structural strains, as explained in Section 5.1.2. However, as this meant it could buckle under small compression loads, corrective measures had to be designed to ensure its stability.

To do this the bending stiffness was increased (increasing the product $E_s I_s$, when E_s is the value of the elasticity modulus of the sensor material, I_s is the moment of inertia of the cross-section) with a system known as a *buckling inhibitor*. In order to avoid the complications described in Section 5.1.2, this system did not modify the value of product $E_s A_s$. The buckling inhibitor restricts movements of the sensor and thus prevents its buckling (Fig.16a) and was designed with the help of an FE model of the sensor on *Lusas* software [20] that provided the sensor's buckling load. This theoretical buckling load was verified experimentally. Fig. 16 shows the model together with the boundary conditions applied. The sensor was simulated by QSL8 type FE elements and the inhibitor by springs with stiffness *K*. The model was used to study the sensor's buckling load (P_{RD}) depending on the inhibitor stiffness according to the method detailed in Section 4.3. For the sensor to operate correctly, this load must be higher than the maximum load supported by the sensor when concrete reaches its ultimate strain (which is 3.5‰ με under bending and axial forces, in accordance with [22]). This load was annotated as $P_{RD,3.5}$. Fig. 17 gives the sensor buckling loads for different sensor lengths and inhibitor stiffness values as well as $P_{RD,3.5}$ values. Minimum inhibitor stiffness for correct sensor operation $E_s I_s$ can be obtained from the graph depending on the sensor length.

From the results displayed in Fig. 17 it can be seen that:

- With no buckling inhibitor the sensor cannot function correctly since it will buckle when subjected to a maximum strain of less than 3.5 ‰.
- As sensor length is increased, inhibitors of higher $E_s I_s$ values must be used. For example, an inhibitor with stiffness 0.4 kN m^2 will solve the buckling problem for sensors up to 40 cm long. However, if the sensor is 60 cm long, minimum sensor stiffness $E_s I_s$ will be 0.6 kN m^2. Finally, an inhibitor with an $E_s I_s$ value equal to kNm^2 will solve this failure mode for sensors up to 100 cm long.

5.2.3 Characteristics of proposed long gauge sensor

In the light of the results of the study, a sensor with the following characteristics is proposed:

- Prismatic cross-sectional area 0.1 cm^2.
- Length between 20 and 100 cm.
- Axial stiffness $E_s A_s = 700$ kN.
- Bending stiffness $E_s I_s$= 58.3 10^{-6}kN m^2.
- Elasticity modulus of adhesive $E_A = 13000\ MPa$.

In these conditions, the measurements obtained from the proposed sensor closely agree with those recorded by the reference sensors (Fig.15). Although certain differences can be observed between both sets of results, these are due to the difficulty of achieving perfectly centered loads on the specimens under test conditions.

6- Conclusions

This paper presents the studies on the design of a new FBG-based long gauge fiber optic sensor, whose principal novelty and advantage is that it does not require prestressing of the optical fiber in order to function correctly. It thus paves the way for the development of fiber optic sensors able to measure strain at extremely high temperatures, such as those found in building fires.

The experimental and numerical studies carried out were able to ensure the correct operation of the sensor and analyzed: 1) the interaction of the sensor with the structure; 2) the influence of the mechanical and geometric properties of its packaging on its ability to measure strains; 3) sensor optimization to reduce measurement errors to a minimum; and 4) the sensor's possible failure modes. The sensor also provided satisfactory results when it was used to monitor structures such as a high-speed rail tunnel in Mogente (Valencia, Spain) [23].

The principal conclusions are as follows:

1) The sensor's anchorage points on the structure must ensure the correct transmission of strains from the host structure to the sensor, which requires the use of an adhesive with an elasticity modulus E_A equal to or above 400 MPa

2) The sensor's axial stiffness (product E_sA_s) should be low enough to allow correct measurements. High E_sA_s values provide inaccurate results as they provide a local strengthening of the structure that alterates the strains of the structure around the sensor. Sensors with $E_sA_s$values lower than 5 MN and a minimum length of 20 cm provide differences between actual and measured strains of less than 4%. However, the influence of the unit's axial stiffness is lower for longer sensors; for example, an E_sA_s value of 20 MN has a measurement error of around 11% when the unit is 20 cm long, while this is reduced to 4% if the length is 60 cm.

3) The sensor may fail due to shear forces in the anchor zone. In this regard it is important to point out the following:

    a. High E_sA_s values will cause shear forces in the anchorage high enough to cause failure. To avoid this it is proposed to use a sensor with an $E_sA_s$value of 700 kN and increased roughness of the contact interface to enhance cohesion at the concrete/sensor interface.

    b. Using adhesive with a high elasticity modulus also causes high shear forces at the interface. Although it may be thought advisable to use adhesives with low elasticity modulus, this entails the disadvantage of incomplete strain transfer and so is not recommended.

4) The proposed sensor may also fail due to buckling. To avoid this, a buckling inhibitor was designed to raise the sensor's E_sI_s value without contributing to its axial stiffness E_sA_s. A sensor unit with a bending stiffness of 1 kNm^2 would solve this problem for sensors up to 100 cm long and for combined bending/compression loads in which the maximum compression strain of the concrete is 3.5‰.

Acknowledgments.

This work was made possible by the support from the *Universitat Politècnica de València*, the Spanish Ministry for Science and Innovation (Research Project BIA2011-27104) and the Spanish Ministry of Public Works (Project Sopromac P41/08).

References:

[1] Glišić B, Inaudi D (2007). "Fibre Optics Methods for Structural Health Monitoring".Chichester: John Wiley & Sons Ltd.

[2] Thomas Kissinger, Thomas O H Charrett and Ralph P Tatam (2013)."Fibre segment interferometry using code-division multiplexed optical signal processing for strain sensing applications". Measurement Science and Technology 24 (2013) 094011 (13pp).

[3] Ada Abangand David J Webb (2014). "Effects of annealing, pre-tension and mounting on the hysteresis of polymer strain sensors".Measurement Science and Technology 25 (2014) 015102 (6pp).

[4] www.alava-ing.es . Accessed on May 27, 2014.

[5] ww.roctest-group.com/ Accessed on May 27, 2014.

[6] Glišić B, Inaudi D, Lau JM (2005). "Long-term monitoring of high-rise buildings using long-gauge fiber optic sensors".7th International Conference on Multi-Purpose High-Rise Towers and Tall Buildings (IFHS), Dubai, United Arab Emirates. (on conference CD, paper #0416).

[7] Glišić B, Inaudi D, Kronenberg P, Vurpillot S (1999). Dam monitoring using long SOFO sensor.Hydropower into the Next Century, Gmunden, Austria.709–717.

[8] Calderón PA,Glisic B (2012). "Influence of mechanical and geometrical properties of embedded long-gauge strain sensors on the accuracy of strain measurement". Measurement Science and Technology 23 065604 (15pp).

[9] Torres B, Payá-Zaforteza I, Calderón P A and Adam J M (2011). "Analysis of the strain transfer in a new FBG sensor for structural health monitoring" Eng. Struct. 33 539–48.

[10] Majumder M, Gangopadhyay TM, Chakraborty AK (2008). "Fibre Bragg gratings in structural health monitoring—present status and applications". Sensors Actuators, 147:150–64.

[11] Li D, Li H, Ren L, Song GB, (2006). "Strain transferring analysis of fiber Bragg grating Sensors". Opt Eng. 2006;45(2):1–8.

[12] Moyo P, Brownjohn JMW, Suresh R, Tjin SC (2005). “Development of fiber Bragg grating sensors for monitoring civil infrastructure”. EngStruct. 27:1828–34.

[13] Leng J S, Winter D, Barnes R A, Mays G C and Fernando G F (2006). “Structural health monitoring of concrete cylinders using protected fiber optic sensors” Smart Mater. Struct.15 302–8.

[14] Kesavan K, Ravisankar K, Parivallal S, Sreeshylam P and Sridhar S (2010). “Experimental studies on fiber optic sensors embedded in concrete”. Measurement43 157–63.

[15] Measures R 2001 Structural Monitoring with Fiber Optic Technology (London: Academic) p 717

[16] Kleckers T; BerndGünther. Bandas ópticas o bandas eléctricas: una comparación.http:/www.hbm.es/custserv/SEURLF/ASP/SFS/ID.802/MM.4,101,180/SE/techarticles.htm. Julio 2007.

[17] Chung W, Kang D. Full-scale test of a concrete box girder using FBG sensing system. EngStruct 2008;30(3):643–52.

[18] Norma UNE 83316 (1996). Ensayos de Hormigón. Determinación del módulo de elasticidad en compresión (In Spanish).

[19] Bueno Martínez A (2008). “Diseño y caracterización de un sensor óptico autocompensado en temperatura para la medida de deformaciones en estructuras de ingeniería civil y desarrollo de un sistema de interrogación”. Tesis Final de Máster. Escuela Técnica Superior de Ingenieros de Telecomunicaciones. Universidad Politécnica de Valencia (In Spanish).

[20] Lusas (2010). Lusas Reference Manual. Surrey (UK).

[21] Adam JM; Antonio Brencich; Tim G. Hughes; Tony Jefferson .Micromodelling of eccentrically loaded brickwork: Study of masonry wallettes. Engineering Structures (2010) 32, 1244-1251.

[22] Eurocode 2. Design of concrete structures.DD ENV 1992-1-1:1992

[23] Benjamín Torres; Ignacio Payá-Zaforteza; David Barrera; Yezid A. Alvarado; Pedro A. Calderón; AlaynLoayssa; Mikel Sagüés; AnderZornoza; Salvador Sales (2014). “High-speed railway tunnel monitoring using point, long gauge and distributed strain and temperature fiber optic sensors”. Informes de la Construcción. Accepted for publication. In Spanish.

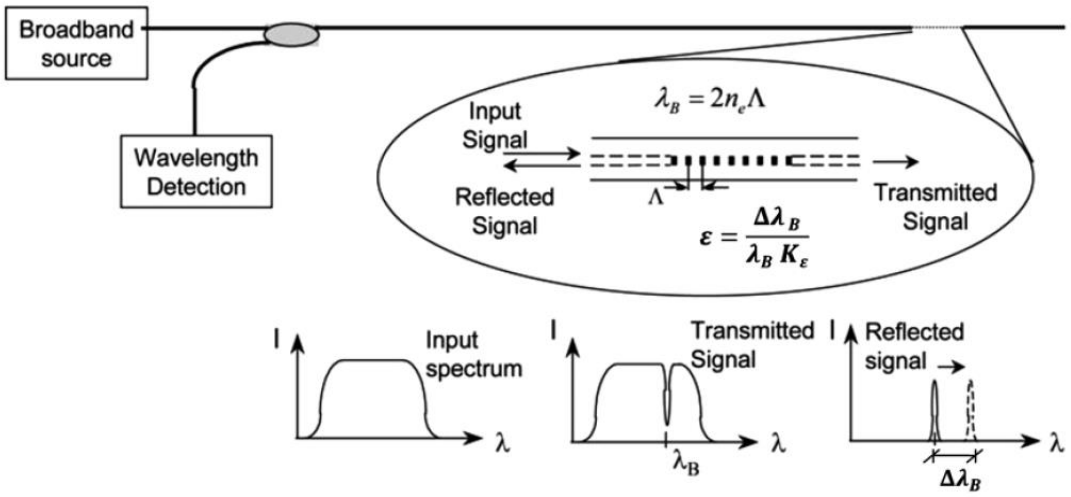

Figure 1. Basic Bragg grating-based sensor system with transmissive or reflective detection options. Based on [17].

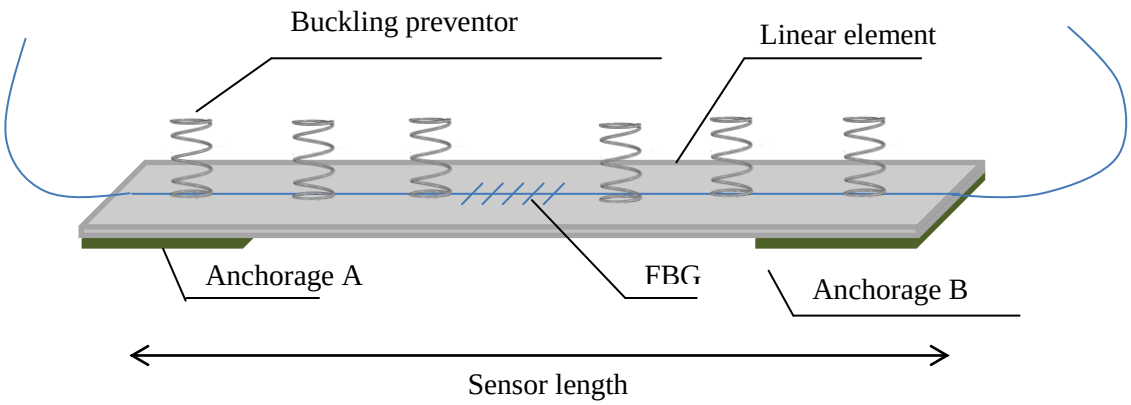

Figure 2. Schematic representation of the new long gauge sensor.

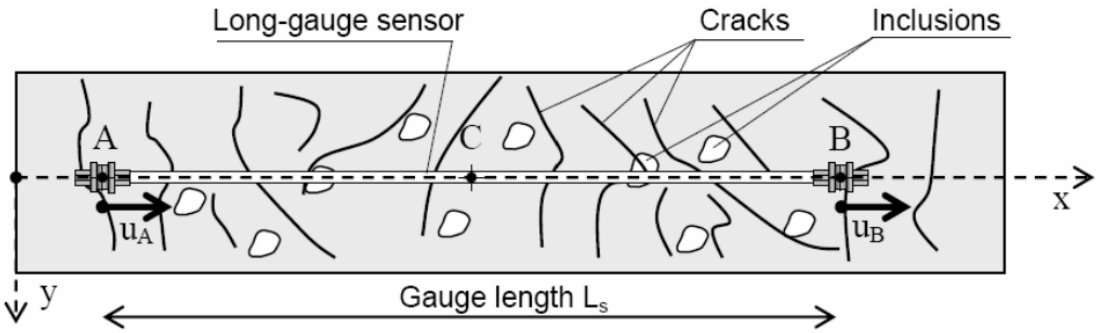

Figure 3. Schematic representation of a long-gauge sensor in an inhomogeneous material (courtesy of SMARTEC SA [5]).

(a) (b) (c)

Figure 4. Types of specimens used to test the long gauge sensors: (a) Specimen with a height of 0.4 m (Specimen A), (b) Specimen with a height of 1 m (Specimen B), (c) Specimen with a height of 3 m (Specimen C).

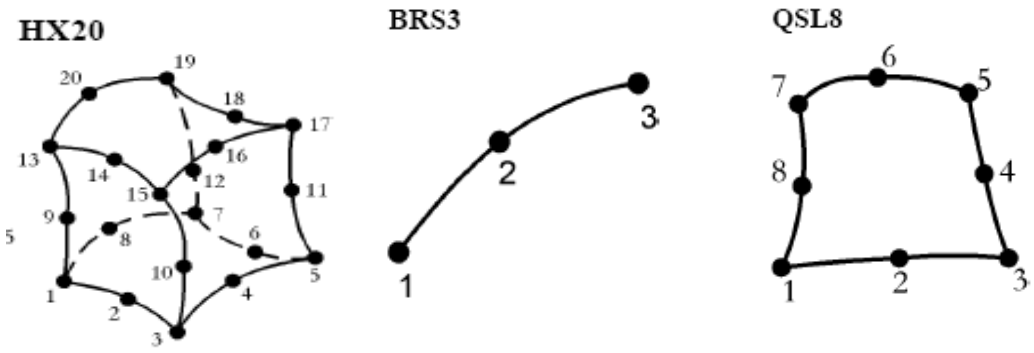

Figure 5. Finite elements used in the numerical models [20].

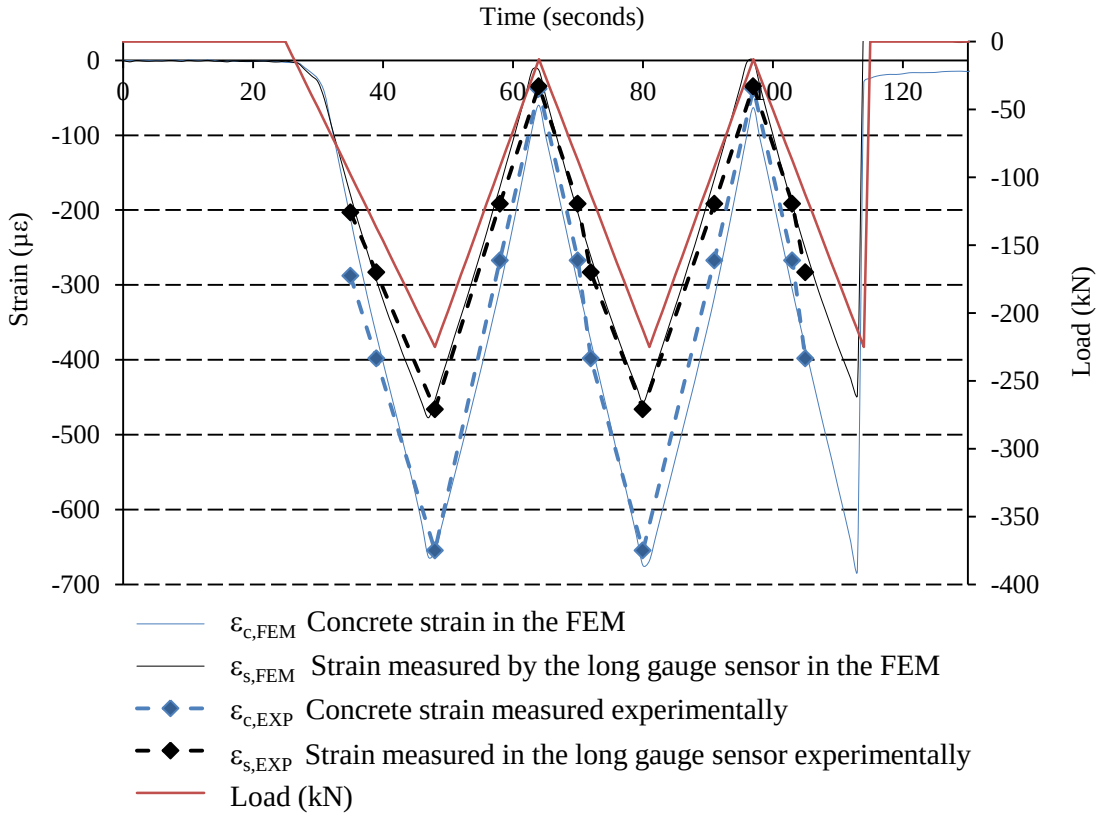

(a)

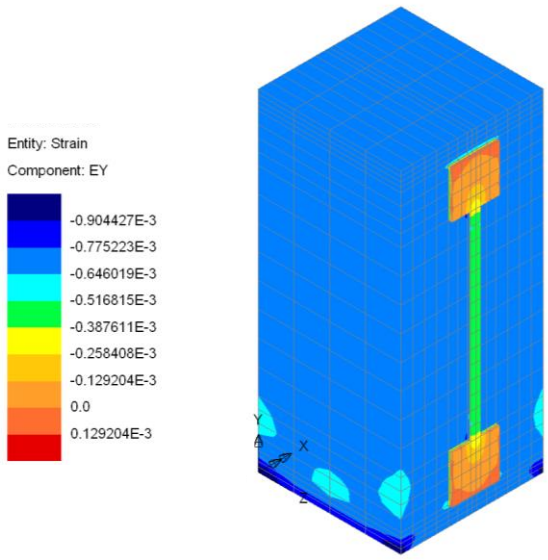

(b)

Figure 6. Specimen A: (a)- Numerical and experimental results of the strains measured in the specimen and sensor and the load cycle applied to the specimen. (b)- Numerical finite element model. $\varepsilon_{s,FEM}/\varepsilon_{c,FEM} \approx 0.75$

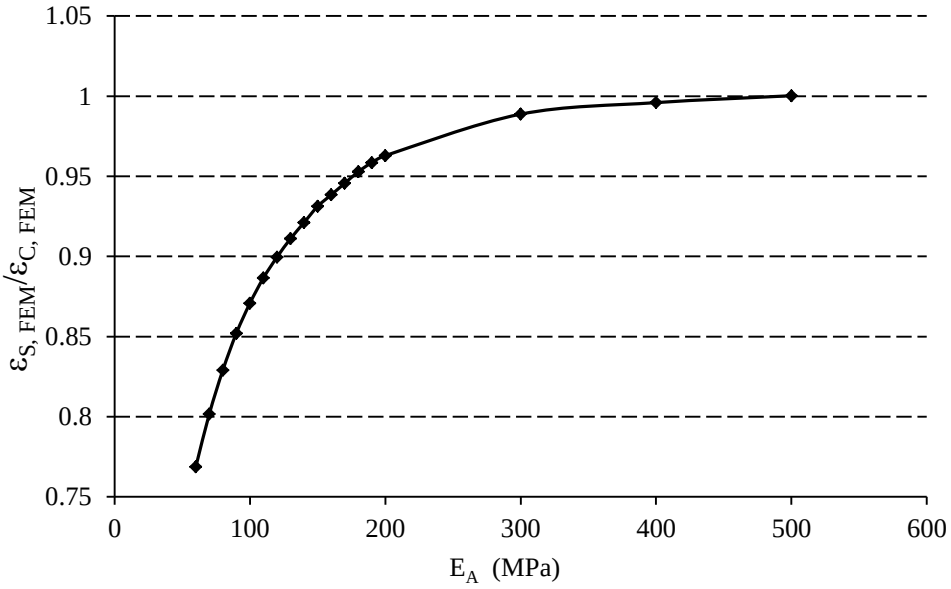

Figura 7. Effect of the adhesive's elasticity modulus E_A on the $\varepsilon_{s,FEM}/\varepsilon_{c,FEM}$ ratio. Compressive stress applied to the top face of Specimen A: 21 MPa

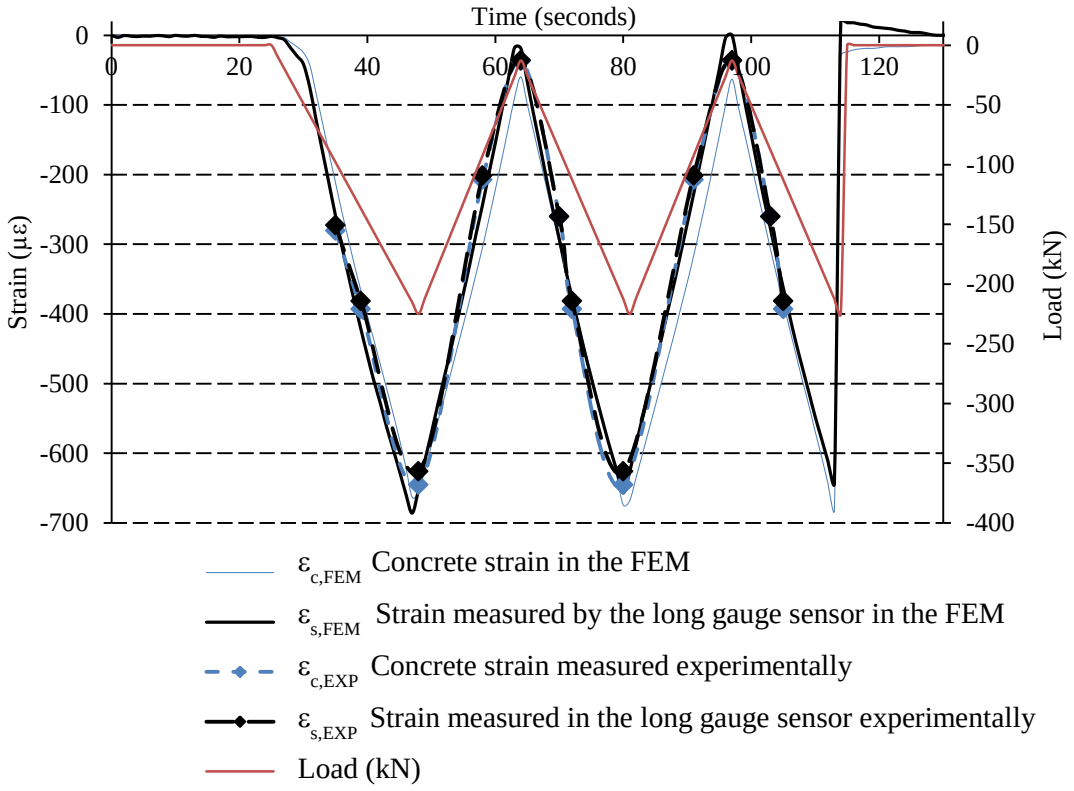

(a)

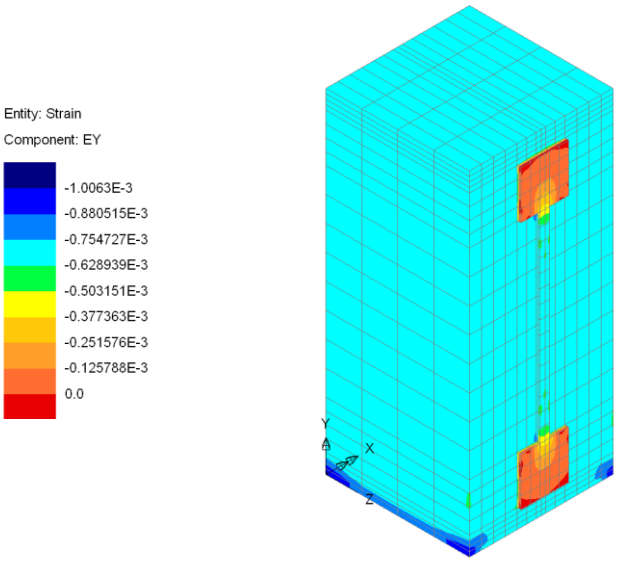

(b)

Figura 8. Specimen A: (a)- Numerical and experimental results of the strains measured in the specimen and sensor and the load cycle applied to the specimen.. (b)- Numerical finite element model. $\varepsilon_{s,FEM}/\varepsilon_{c,FEM} \approx 1$

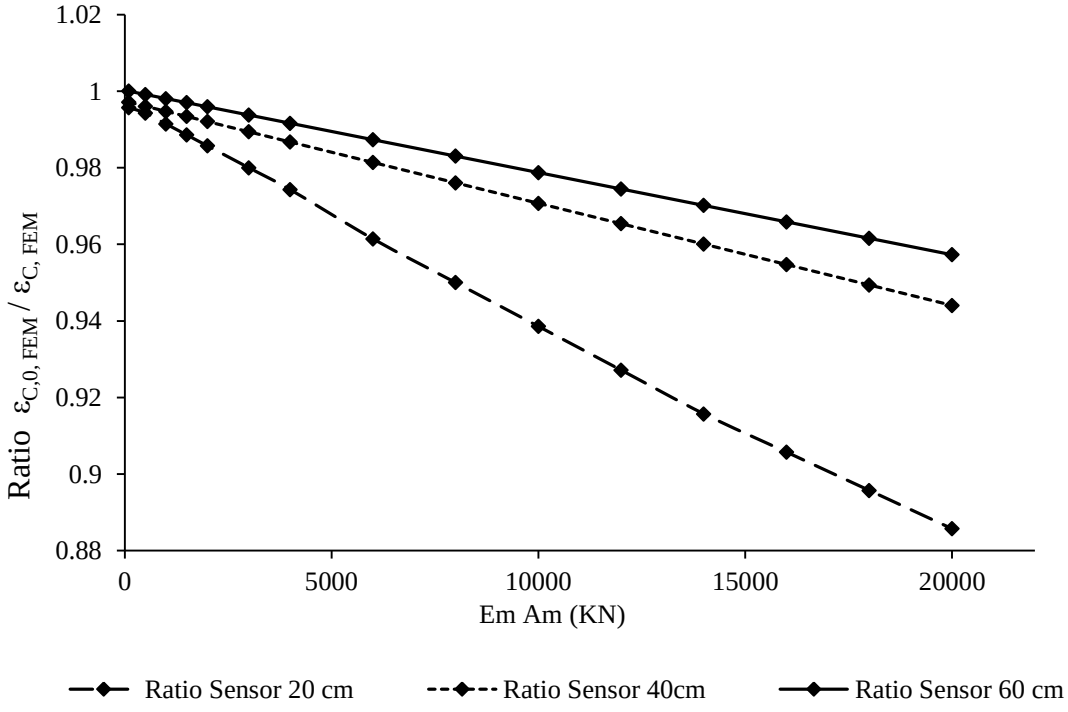

Figura 9. Influence of axial stiffness $E_s A_s$ on the $\varepsilon_{C,0,FEM}/\varepsilon_{c,FEM}$ ratio. Compressive stress applied to the top face of specimen A: 21 MPa. Value of adhesive's elasticity modulus E_A = $13\ 10^3\ MPa$

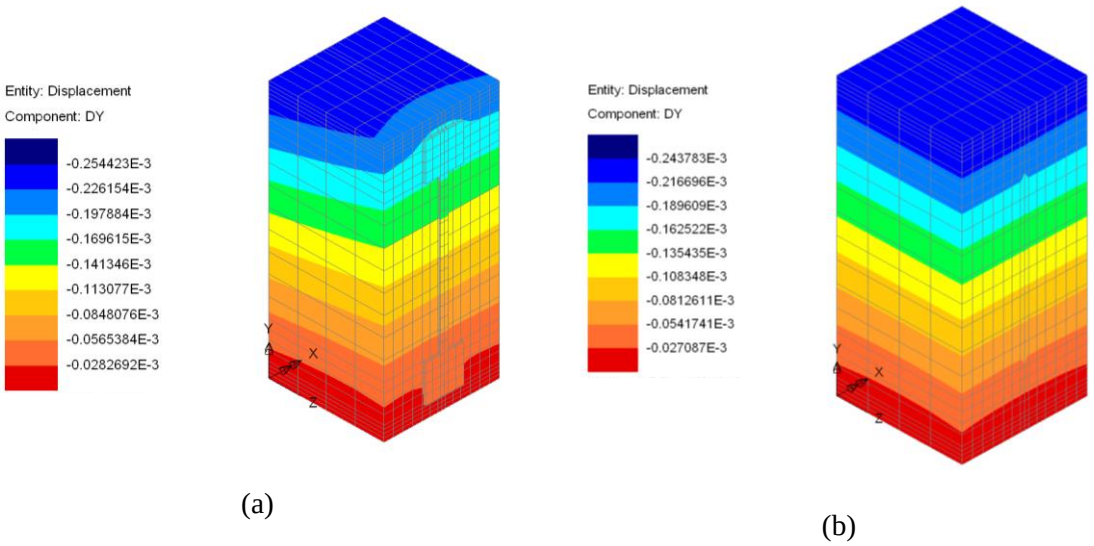

(a) (b)

Figure 10. Y axis displacements (m): (a)- with a sensor with axial stiffness $E_s A_s$ =10000 kN. (b)- without any sensor.

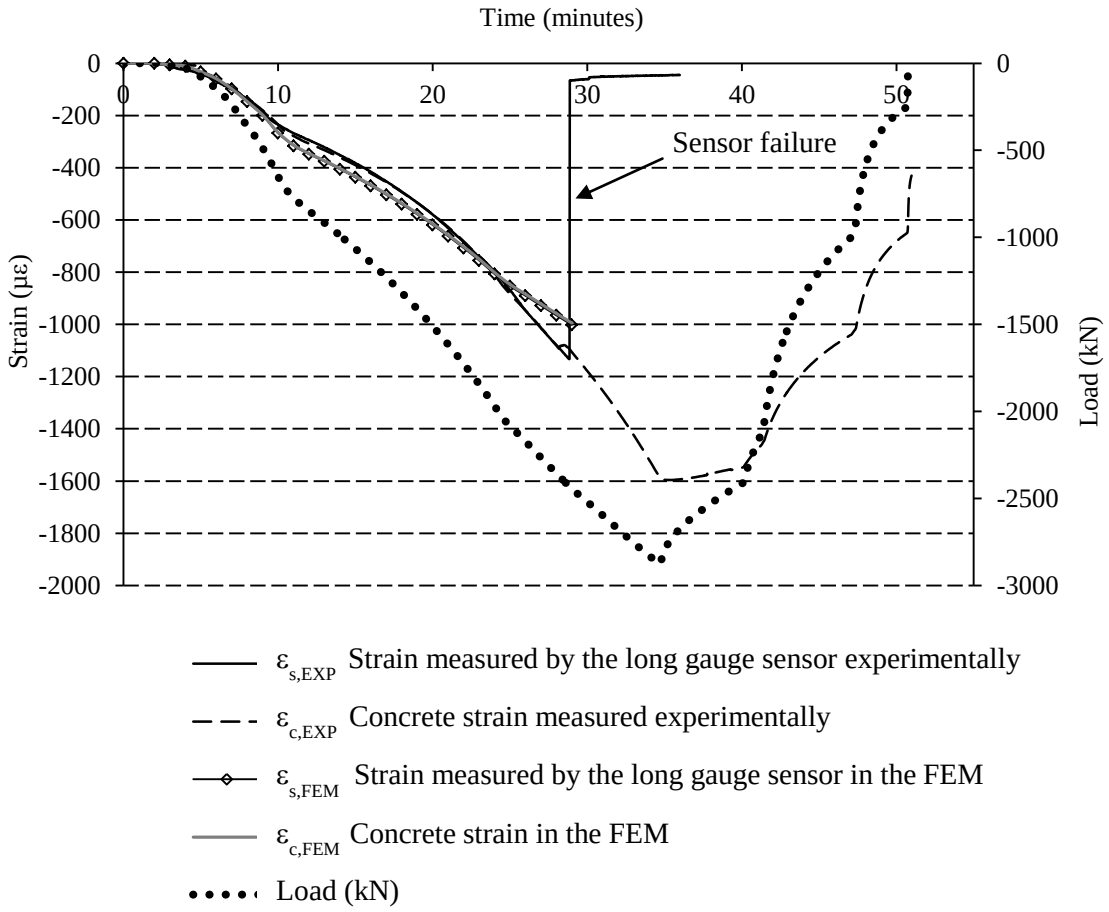

Figura 11. Numerical and experimental results of a simple compression test on a 3 m high column described in Section 3.1 (Specimen C)

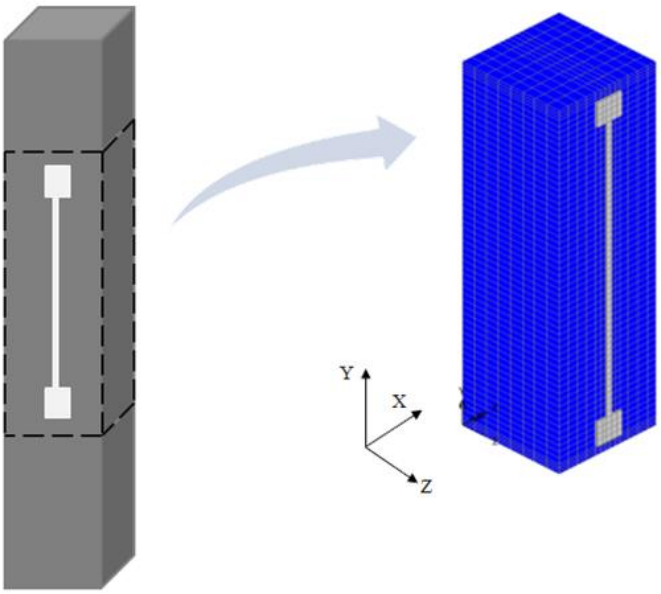

(a)

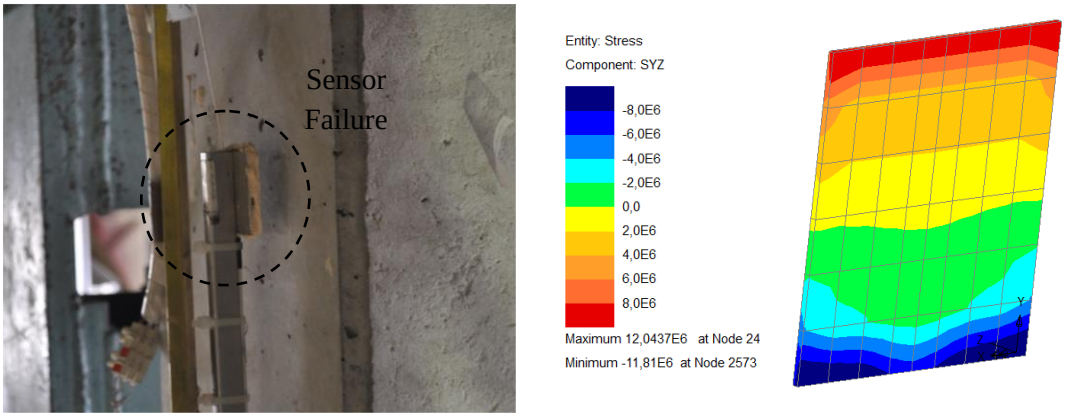

(b)

Figure 12. (a) Frontal view of concrete specimen.
(b)- Sensor failure. Finite element model of sensor/concrete interface. When failure took place, the value of the shear stress at the interface was equal to 12.04MPa.

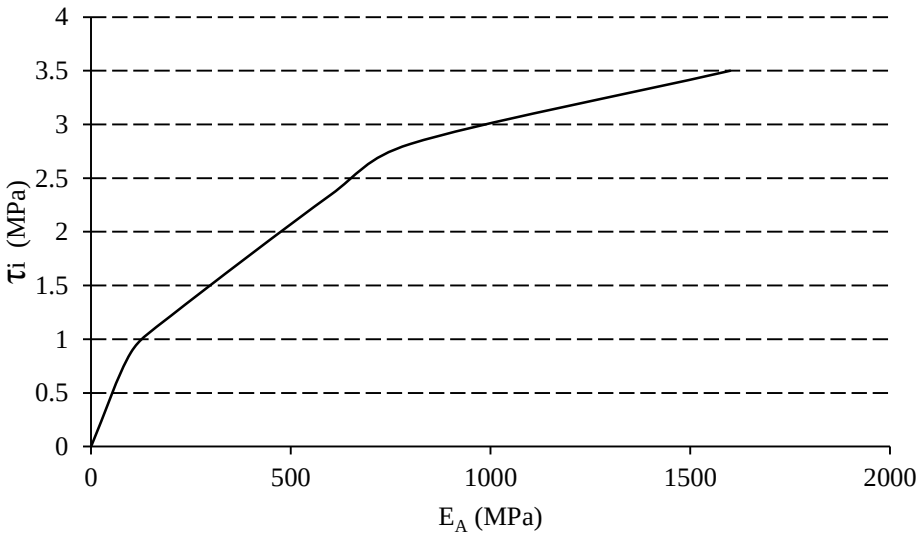

Figure 13. Shear stress τ_i at the concrete-adhesive interface depending on the adhesive elasticity modulus E_A.

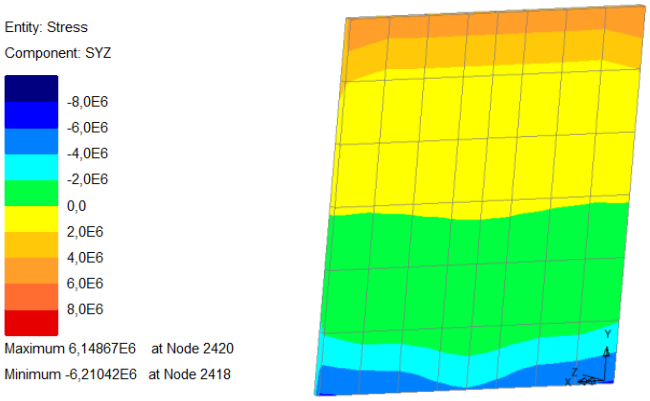

Figure 14. Shear stresses (maximum value equal to 6.15 MPa) at the concrete-adhesive interface.

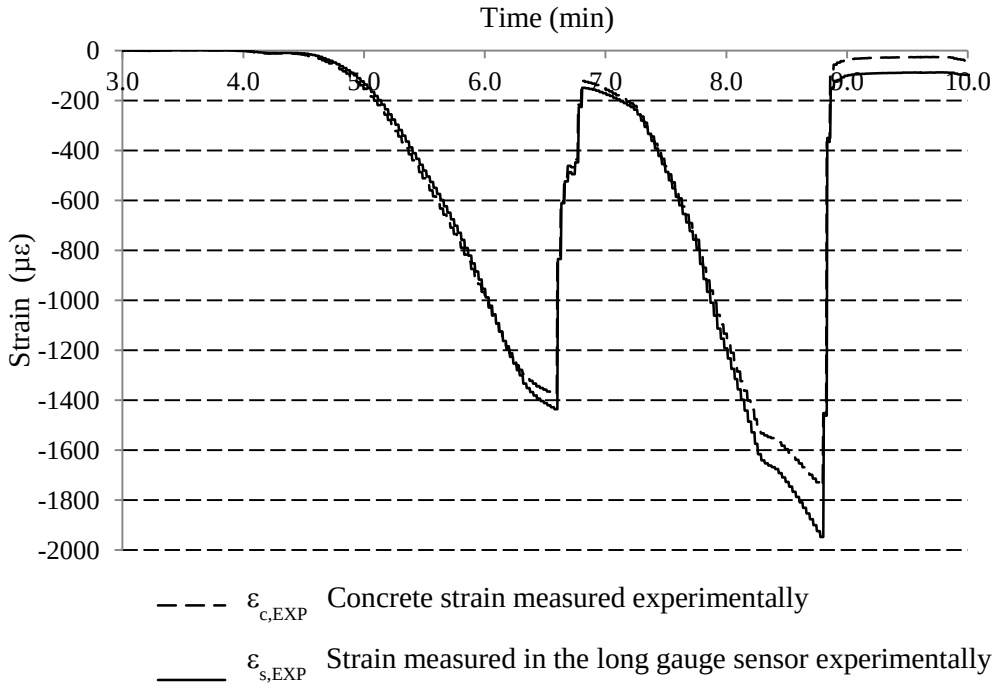

Figure 15. Results of the experimental test. Conducted with Specimen C.

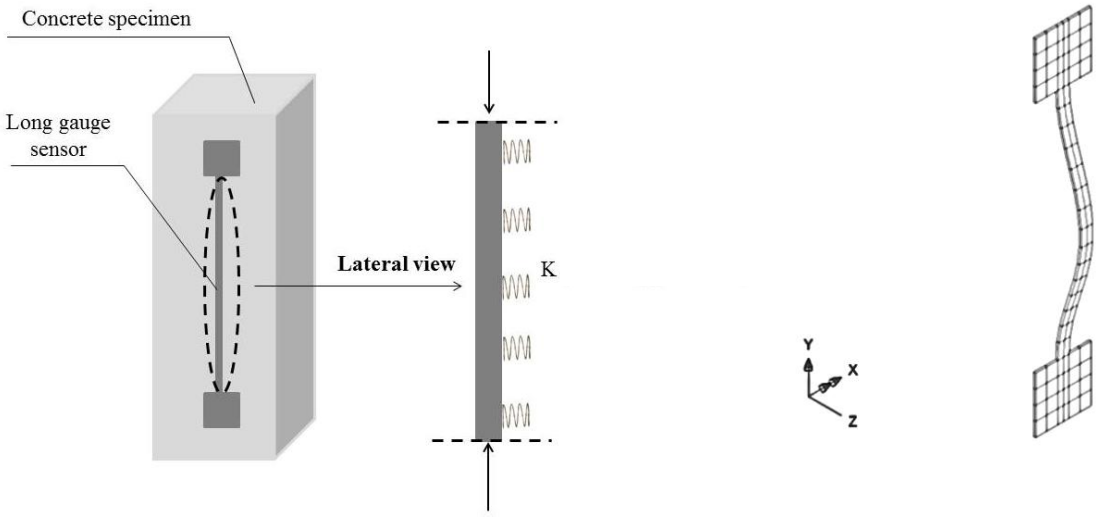

(a) (b)

Figure 16. (a)- Sensor and modeling of the buckling inhibitor with a spring of stiffness *K* (b)- Deformed mesh of the sensor under compression loads. First buckling mode.

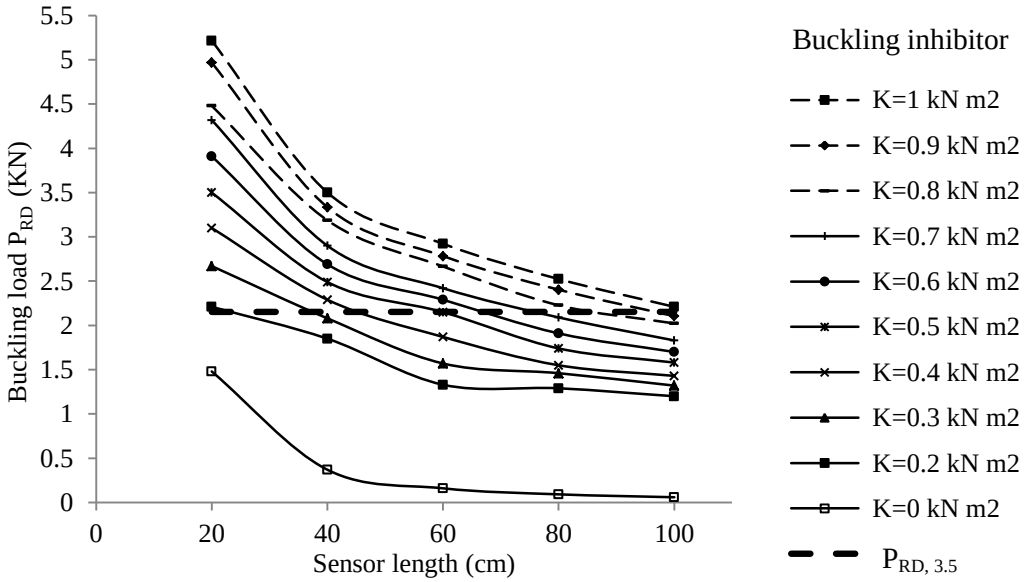

Figure 17. Buckling loads depending on the relative stiffness of the buckling inhibitor and the long gage sensor lengths.

Specimen	Specimen dimensions (m)	Goals of the test
Specimen A (Figure 4.a)	0.1 x 0.1 x 0.4	Strain transfer (Section 5.1.1) Axial stiffness $E_s A_s$ (Section 5.1.2)
Specimen B (Figure 4.b)	0.2 x 0.2 x 1.2	Anchorage failure (shear stress) (Section 5.2.1) Sensor buckling (Section 5.2.2)
Specimen C (Figure 4.c)	0.3 x 0.3 x 3	Anchorage failure (shear stress) (Section 5.2.1)

Table 1. Relationship between the type of specimen tested and the goals of the study.

Cylindrical Specimen	**Concrete compressive Strenght, f_c (MPa)**	**Young´s Modulus, E (MPa)**
1	106.6	35350
2	98.2	33824
3	96.5	33176
Average	100.4	34116

Table 2. Specimen A (Fig.4). Values of concrete compressive strength and Young's Modulus.

Cylindrical Specimen	**Concrete compressive strenght, f_c (MPa)**	**Young´s Modulus E (MPa)**
1	37.4	30330
2	36.8	29664
3	-	28356
Average	37.1	29450

Table 3. Specimens B and C (Fig. 4). Values of concrete compressive strength and Young's Modulus.

Contact interface	$\mathbf{E_P^S}$ **(MPa)**	$\mathbf{E_N^S}$ **(MPa)**	$\mathbf{G_P^S}$ **(MPa)**	$\mathbf{G_N^S}$ **(MPa)**	$\boldsymbol{\upsilon_P^S}$	$\boldsymbol{\upsilon_N^S}$	$\mathbf{c_s}$ **(MPa)**	$\boldsymbol{\phi_s}$ **(°)**	$\mathbf{f_t}$ **(MPa)**
Concrete-adhesive	$21.25\ 10^3$	$21.25\ 10^3$	$8.17\ 10^3$	$8.17\ 10^3$	0.3	0.3	10-15	0	35

Table 4. Properties of the concrete-adhesive interface used in the FE model.

Test	L_s (m)	E_A (MPa)	A_m (cm^2)	$\tau_{i,}$(MPa)	$\varepsilon_{c,FEM}$ ($\mu\varepsilon$)	$\varepsilon_{s,FEM}$ ($\mu\varepsilon$)
1	1	13000	0.2	12.04	-1001.9	-994.7
2	1	13000	0.1	6.15	-979.5	-970.3

Table 5. Main data and results obtained with the FE model at failure when the sensor fails by separation due to shear stress. Sensors with A_m = 0.2 cm^2 (Test 1) and with A_m = 0.1 cm^2 (Test 2).